Design and Experimental Evaluation of a 256-Channel Dual-Frequency Ultrasound Phased-Array System for Transcranial Blood–Brain Barrier Opening and Brain Drug Delivery

Hao-Li Liu*, *Member, IEEE*, Chen-Kai Jan, Po-Chun Chu, Jhong-Cing Hong, Pei-Yun Lee, Jyh-Duen Hsu, Chung-Chih Lin, Chiung-Ying Huang, Pin-Yuan Chen, and Kuo-Chen Wei*

***Abstract*—Focused ultrasound (FUS) in the presence of microbubbles can bring about transcranial and local opening of the blood–brain barrier (BBB) for potential noninvasive delivery of drugs to the brain. A phased-array ultrasound system is essential for FUS-BBB opening to enable electronic steering and correction of the focal beam which is distorted by cranial bone. Here, we demonstrate our prototype design of a 256-channel ultrasound phased-array system for large-region transcranial BBB opening in the brains of large animals. One of the unique features of this system is the capability of generating concurrent dual-frequency ultrasound signals from the driving system for potential enhancement of BBB opening. A wide range of signal frequencies can be generated (frequency = 0.2–1.2 MHz) with controllable driving burst patterns. Precise output power can be controlled for individual channels via 8-bit duty-cycle control of transistor–transistor logic signals and the 8-bit microcontroller-controlled buck converter power supply output voltage. The prototype system was found to be in compliance with the electromagnetic compatibility standard. Moreover, large animal experiments confirmed the phase switching effectiveness of this system, and induction of either a precise spot or large region of BBB opening through fast focal-beam switching. We also demonstrated the capability of dual-frequency exposure to potentially enhance the BBB-opening effect. This study contributes to the design of ultrasound phased arrays for future clinical applications, and provides a new direction toward optimizing FUS brain drug delivery.**

***Index Terms*—Blood–brain barrier (BBB), dual frequency, focused ultrasound (FUS), phased array.**

Manuscript received May 6, 2013; revised December 31, 2013 and February 4, 2014; accepted February 8, 2014. Date of publication February 11, 2014; date of current version March 17, 2014. This work was supported in part by National Science Council Grants No. 100-2321-B-182-010-, 101-2321-B-182-015-, 101-2221-E-182-002-MY3, and NSC 102-2120-M-182A-002. *Asterisks indicate corresponding authors.*

*H.-L. Liu is with the Department of Electrical Engineering and Biomedical Engineering Center, Chang-Gung University, Taoyuan 333, Taiwan (e-mail: haoliliu@mail.cgu.edu.tw).

C.-K. Jan, P.-C. Chu, J.-C. Hong, P.-Y. Lee, and J.-D. Hsu are with the Department of Electrical Engineering and Biomedical Engineering Center, Chang-Gung University, Taoyuan 333, Taiwan (e-mail: whatdavid@yahoo.com.tw; bargsonchu@gmail.com; haoliliu@gmail.com; jdheric@gmail.com; sharonsea7474@gmail.com).

C.-C. Lin is with the Department of Computer Science and Information Engineering, Chang-Gung University, Taoyuan 333, Taiwan (e-mail: cclin@mail.cgu.edu.tw).

C.-Y. Huang and P.-Y. Chen are with the Department of Neurosurgery, Chang-Gung University and Memorial Hospital, Taoyuan 333, Taiwan (e-mail: chyinhuang@adm.cgmh.org.tw; pinyuanc@adm.cgmh.org.tw).

*K.-C. Wei is with the Department of Neurosurgery, Chang-Gung University and Memorial Hospital, Taoyuan 333, Taiwan (e-mail: kuochenwei@adm.cgmh.org.tw).

Color versions of one or more of the figures in this paper are available online at http://ieeexplore.ieee.org.

Digital Object Identifier 10.1109/TBME.2014.2305723

I. Introduction

It has been confirmed that focused ultrasound (FUS) burst tone exposure in the presence of microbubbles induces local and reversible blood–brain barrier (BBB) opening [1]–[4]. This transcranial procedure opens a new frontier to explore the noninvasive delivery of over 95% of therapeutic molecules that were originally incapable of penetrating across the BBB into the brain. A number of preclinical studies have already demonstrated the feasibility of FUS-BBB opening for enhancing chemotherapeutic agent delivery [5]–[7], gene delivery [8], [9], monoclonal antibody delivery [10], or even the delivery of stem cells [11], suggesting the exciting prospect of developing this technique to perform noninvasive CNS therapy in a clinical setting.

Multiple-element ultrasound phased array is an attractive approach for therapeutic FUS applications. Unlike a single-element transducer with fixed focus at the geometric center, an ultrasound phased array can steer the focus of the ultrasonic energy to an arbitrary position by driving each element with a signal of the appropriate phase. Dynamic focal beam scanning can thus be achieved by electronically altering the relative phases of the elements' signals. The relative phase of each element is independently controlled, and interference of the generated radio-frequency (RF) driving signals result in generation of focal beam energy spatially surrounding the geometrical center. Moreover, since the phase switch is controlled by the electrical signal control of the driving system, high speed switching of the ultrasound energy, and therefore high-speed focal scanning, becomes possible. Such ultrasound phased-array systems are increasingly being used for clinical applications. Buchanan *et al*. proposed a 64-channel, 500-kHz, continuous wave (CW) mode phased-array system for transrectal thermal ablation [12]. Daum and Hynynen [13] designed a 256-element phased-array system for use in CW mode with a 1.1-MHz spherically curved phased array for abdominal thermal ablation. For brain application, Clement *et al*. first presented the concept of hemispherical ultrasound phased-array design [14]. Pernot *et al*. [15] also showed that a multiple element hemispherical

array operating at a frequency of 1 MHz can successfully generate targeted thermal lesions through an intact animal skull after applying focus-restoring technology. In addition, Clement *et al*. and Hynynen *et al*. developed CW 500-element driving systems for use with hemispherical phased arrays operating at 700–800 kHz for brain–tissue thermal ablation [16], [17].

Adaptation of the current thermal-ablation-based ultrasound phased-array system for the application of FUS BBB opening requires a different design of the selection of driving frequency. The center frequency for clinical thermal ablation should be at least 0.8 MHz to provide suitable tissue-heat absorption for the required elevation in temperature [18]–[20]. On the other hand, the application of FUS in BBB opening requires an operating frequency which results in less heat absorption by bone and fewer cranial ultrasound aberrations/distortions. Moreover, unlike the CW mode ultrasound energy exposure of thermal ablation, the ultrasound energy required for BBB opening needs to be the repetitive burst tone type exposure so that microbubbles can be back-filled in the next circulation cycle [4], [21]. Temporal disruption of the BBB relies on this microbubble-ultrasound interaction which induces tight-junction and endothelial cell deformation [22]. We previously developed a low-frequency hemispherical ultrasound phased-array system (260 kHz, 32-channel) for BBB opening, and demonstrated its successfully application [23]. Recently, Song *et al*. also investigated the use of a commercial 1011-element, 230 kHz hemispherical ultrasound phased array for the purpose of transcranial ultrasound beam steering [24]. A number of other recent studies have also demonstrated induction of a relatively large area of BBB opening by either electronic or mechanical steering with multiple sonication cycles at different adjacent target positions (for example 3×3 matrix sonication) [25], [26], thus confirming the importance of ultrasound phased-array technology for CNS drug delivery.

Up to date, FUS-induced BBB opening has been limited to single-frequency exposure, regardless of whether a phased array or single element transducer was used. However, dual frequency ultrasound has been successfully applied in other applications and is well known to enhance acoustic cavitation as measured by enhanced subharmonic/ultraharmonic emissions (an indication of stable cavitation), enhanced wideband emissions/enhanced hydrogen peroxide in the medium (an indication of inertial cavitation), or bubble enrichment (a macroscopic bubble/cavitation effect) [27]–[29]. Previous studies have demonstrated the enhancement of stable cavitation by dual-frequency exposure, both with and without microbubbles [29], [30]. The enhanced cavitation effect due to dual-frequency ultrasound exposure has also been shown to enhance the anticancer effect (1 MHz/150 kHz) [31], skin permeability (frequency combination ranging from 20 to 3 MHz) [32], and drug delivery (70/500 kHz) [33]. We also previously demonstrated the use of single-element ultrasound to achieve dual-frequency excitation to enhance acoustic cavitation [28]. For the application of brain drug delivery, acoustic cavitation is already known to be highly correlated with the degree of FUS-induced BBB opening [34]. Therefore, the use of dual-frequency exposure with a phased-array system design could potentially allow further manipulation of the BBB-opening process to increase brain drug delivery.

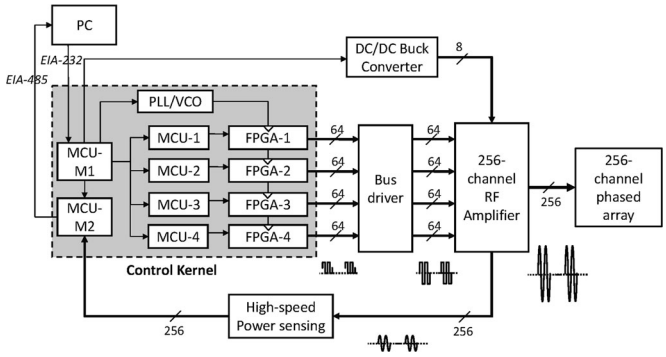

Fig. 1. Block diagram of the circuit structure of the 256-channel ultrasound brain drug delivery driving system.

The aim of this study was to demonstrate our prototype design of a novel 256-channel ultrasound phased-array driving system capable of both dual-frequency excitation and induction of large-scale transcranial BBB opening via electronic steering. A key feature of the system design is its capability of simultaneously generating multiple frequency outputs. A 256-channel low-frequency ultrasound driving system was designed to provide a suitable acoustic output for BBB opening. The phased array was spherically curved to allow delivery of concentrated ultrasonic energy into the brain. The performance of the FUS phased array was evaluated. Theoretical predictions were used to optimize the design of the phased array and compare its performance with the experimental data. Large animal experiments and histological examinations were conducted to assess the ability of the phased-array system to disrupt the BBB.

II. Methods

A. Cascade-Microcontroller/Field-Programmable-Gate-Array (MCU/FPGA)-Based 256-Channel Dual-Frequency Control Kernel Design

The design overview and photographs of the 256-channel ultrasound phased-array driving system are shown in Figs. 1 and 2. The system consists of three major circuit modules: the control kernel, the multiple channel RF driver, and the multiple channel high-speed power sensor feedback.

For the control kernel, we modified our previous design [23] by using an MCU/FPGA-based embedded system structure which generated 256-channel phasing transistor–transistor logic (TTL) signal outputs (see Fig. 1). MCUs were used to communicate with the down-stage FPGAs for phasing and control of output parameters. Commercially available 8-bit units (PIC 18 F 452, Microchip, Chandler, Arizona, USA) were used as MCUs. Two master MCUs and four slave MCUs were embedded in the control kernel. The purpose of the first master MCU (denoted MCU-M1) was: 1) to serve as the communication unit with the PC through the universal synchronous–asynchronous receiver transmitter (USART) EIA-232 protocol operated in "transmit" mode; and 2) to provide voltage control for power output

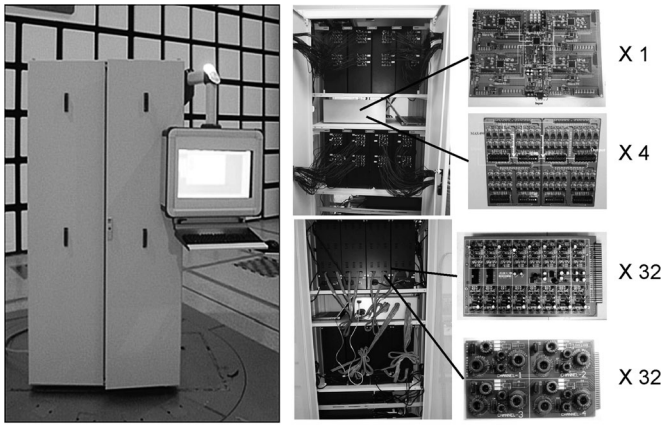

Fig. 2. Appearance of (a) system cabinet and (b) circuit composition of the 256-channel ultrasound phased-array driving system. The system consists of a single control kernel board, one differential TTL output board, 32 dc-to-ac inverter boards, and 32 matching and power sensing boards. In addition to the designed circuit board, four sets of MCU-controlled buck dc-to-dc converters in conjunction with four power supplies were installed in the system cabinet.

regulation through a voltage-controlled buck converter via pulsewidth modulation (PWM) control.

The purpose of the second master MCU (denoted MCU-M2) was to provide power feedback from the power sensing module from each driving channel connected to a multiplexor network. This network could sequentially sense the forward and reflected power through the 8-channel A/D converter on the MCU (via the directional coupler). Each MCU A/D input channel was connected to a two-stage 8-to-1 multiplexer (MUX HEF 4067 B, NXP Semiconductor) that together provided 256 forward and another 256 reflected power sensing channels, i.e., a total of 512 channel feedback signals for each MCU A/D input pin. The PC and MCU-M2 communicated in the USART EIA-485 "receive" mode to sequentially transmit the 256-channel forward and 256-channel reflected power data back to the PC for real-time display of individual high-speed power information.

Four PIC1 8 F 452 MCUs were used as slave-MCUs (denoted MCU-1 to MCU-4), each serving as a 64-channel TTL phasing output to the RF driving modules. The four slave-MCUs received multiple groups of phasing signals from MCU-M1 (through the interintegrated communication protocol), and communicated with the downstream FPGA integrated circuits (ICs) (CY 22395 FC, Altera, USA) to assign the phase difference among the channels from the 8-bit parallel I/O ports. Details of the implementation of phasing signal generation have been previously described [23].

In order to rapidly switch different phasing signals on each transducer element for fast focal beam scanning, multiple phasing groups were recorded in the FPGA memory slots and a synchronizing trigger signal from MCU-M1 controlled simultaneous switching of the phasing information in the four FPGAs. Burst-tone mode excitation was achieved by a simple latch circuit in the FPGA which generated RF output with a controllable burst length signal ranging from 0.1 to 999.9 ms at a resolution of 0.1 ms. Besides burst length, the pulse-repetition frequency (PRF), total burst number, and total exposure time could also be controlled from the PC.

The system was designed to have a tunable operation frequency and to be capable of simultaneously generating output from multiple operating frequencies. In this study, we implemented dual frequency output. The system included a phase-locked loop (PLL)/voltage-controlled oscillator (VCO) IC (CY 22395 FC, Cypress Semiconductor, Inc.) with multiple VCOs generating clock output. Since the maximum clock frequency generation of PLL/VCO IC was 200 MHz, the programmed FPGA produced TTL phasing signals ranging from 200 kHz to 1.2 MHz, resulting in 6-bit phase resolution (i.e., phase resolution of 5.625° per channel). The ability to select either the $F_{\mathrm{VCO},1}$ or $F_{\mathrm{VCO},2}$ clock in an individual channel allowed the 256-channel control kernel to simultaneously generate two distinct operating frequency TTL signals, thereby functioning as a 256-channel dual-frequency ultrasound phased-array system.

B. Wideband RF Driving/High-Speed Power Sensing Design

The driving circuit in each channel comprised three parts: An MCU-controlled dc-to-dc buck converter, an RF amplifier, and high-speed power sensing. A MCU-controlled dc power supply with a maximum total electrical power output of 1000 W was designed in-house. The output dc voltage was supplied from an in-house designed MCU-controlled dc-to-dc buck converter (input voltage = 50 V, output voltage = 5–25 V), and was controllable by PWM signals from the MCU. To ensure the stability of the output power, the MCU received feedback from the output dc voltage. Output voltage was adjustable at the control panel. The maximum power output was designed to be 20 W for each channel.

The output power of the system could be regulated by the PWM-controlled buck dc supply, as well as the control kernel, which provided the flexibility to generate TTL output with various duty cycles (ranging from 30% to 50%, 8-bit resolution; 50% duty cycle represents symmetrical TTL signal output). The PWM-controlled buck dc voltage served as the primary output power designation, and the duty cycle control for individual TTL output signals served as a secondary power regulation route, especially for calibration of the power during operation.

The RF amplifier was designed so that the 256-channel TTL phasing signal (3.3 V) could be fed into differential amplifier modules to gain current driving capability (5 V). A half-bridge dc-to-ac inverter constructed by high-voltage MOSFETs was used to generate a high-voltage square wave, and high-voltage diodes were used to deal with high-voltage switching transients. A transformer-type *LC* oscillating module was connected to allow a high-voltage inverter to transform the high-voltage square wave into a high-voltage sinusoidal wave that matched the ultrasound phased-array element (typically with impedance of several kilohm).

Finally, we designed a high-speed power sensing module based on directional coupler technology [11], [21]. We used eight directional couplers, each providing power sensing for 256 channel outputs including forward and reflected power. Power-dependent forward and reflected voltage sensing from

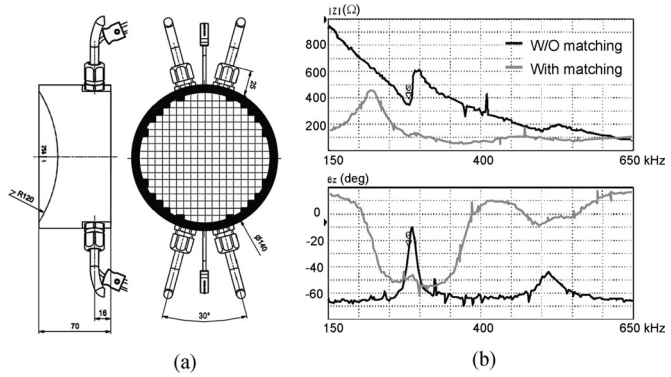

Fig. 3. (a) 256-channel spherical ultrasound phased array (frequency = 400 kHz). (b) Impedance (upper: magnitude, lower: phase) of the transducer element before and after matching, as measured with an impedance analyzer.

the coupler was fed sequentially into the MCU from two-stage 64-to-1 multiplexers via A/D conversion. The data transmission rate of 9600 bit/s allowed the system to receive 256-channel forward/reflected power information at up to 2 frames/s. A rate of 1 frame/s was found to be sufficient for the purpose of real-time power monitoring in this study. Voltage standing-wave ratio (VSWR) was employed to serve as a measure of electrical power transmission efficiency (described in detail in our previous system design [23]).

C. 256-Channel Spherically-Curved Phased Array

A spherically-curved ultrasound phased array was used for the demonstration, measurement, and *in vivo* large animal experiments of the 256-channel driving system (F-number = 1; Imasonic, Inc., France). The phased array was of piezocomposite type with a frequency of 400–800 kHz, diameter of 120 mm, and a curvature radius of 120 mm, diced into 5.5 $\times$ 5.5 mm elements [see Fig. 3(a)]. In impedance matching, the transformer-type impedance transformation configuration was employed to provide wideband (400–800 kHz) power transmission [see Fig. 3(b)]. The transducer dimensions were originally designed to fit a human head and could be used for swine applications (distance between parietal to temporal bone in swine is less than 80 mm).

D. Acoustic Pressure Measurement, Prediction, and Beam Steering Calibration

The free-field pressure field and pressure decay after transmitting FUS through three human cranial bones were measured as previously described [22]. A 3-D positioning table with a polyvinylidene-difluoride (PVDF) type hydrophone (Onda, Sunnyvale, California, USA; calibration range: 50 kHz to 20 MHz) was used to measure the pressure distribution induced by the spherically curved ultrasound phased arrays. The spatial resolution was 0.5 mm in radial directions (denoted as the X- and Y-axes) and 1 mm in the axial direction (denoted as the Z-axis), with maximum measured distances of 40 and 120 mm, respectively. The maximum measured acoustic pressure was 2 MPa, which was equivalent to 300 W of electrical power output (for all channels). To steer the ultrasonic energy at the geometric center, all channels of the driving system were driven in the same phase. Focus steering at a position off the geometric center was based on simple echo traveling and beamforming criteria described previously [13]. For all measurements, the measured distance between the inner skull (either swine or human) and the PVDF hydrophone was fixed at 15 mm for all locations.

In addition to the pressure field measurement, the acoustic pressure distribution from the spherically curved phased array was also predicted theoretically in the free-field case, using the Rayleigh–Sommerfeld integral [22], [35] through the finite-difference-based numerical implementation of MATLAB (Mathworks, Natick, MA). To evaluate the influence of the skull during transcranial delivery of FUS energy into the brain, we investigated the pressure loss caused by the inserted skulls. The calibrated ultrasonic pressure and focal beam dimensions were measured both with and without four harvested swine skulls and in three human cadavers. In transcranial focal-beam pressure measurements, skulls were immersed in a degassed water tank, with the transducer fixed by the stage and PC-programmed orientation-fixed, 2-D translations were performed (i.e., without tilting transducer nor skull). The transmission efficiency was defined as the ratio of the measured pressure with skull insertion to free-field pressure (in %; randomly selected 8 and 50 positions for each swine and human skull, respectively).

E. Electromagnetic Compatibility (EMC) Testing

The 256-channel ultrasound driving system was also used to perform electromagnetic (EM) immunity and EM emission testing to evaluate its EMC (Electronics Testing Center, Taoyuan, Taiwan). EM emission after testing was found to be in compliance with the class-A, group-1 type, CISPR 11 electromagnetic interference (EMI) standard. The system passed the tests for radiated disturbance, disturbance power, harmonic current emission, and voltage fluctuations (based on IEC61000-3-2), as well as flicker (based on IEC61000-3-3). The system also passed EM immunity tests of electrostatic discharge, radiated RF EM fields, electrical fast transient and bursts, surges, conducted disturbances (induced by RF fields), voltage dips/interruptions/variations, power-frequency magnetic field, and power frequency variation immunity.

F. In Vivo Animal Experiments

The BBB opening effect induced by our 256-channel focused driving system was tested in a total of ten swine (body weight 5–8 kg). All animal procedures were approved by the Institutional Animal Care and Use Committee of Chang-Gung University. Animals were anesthetized with isofluorane. The top of the cranium was shaved with clippers, and a PE-50 catheter was inserted into the ear vein for injections. During FUS treatment, ultrasound microbubbles were constantly infused through the ear vein (SonoVue, Bracco Diagnostics, Inc., Milan, Italy) at 0.3 mL/kg/min. The spherically curved 256-element ultrasound phased array was employed for animal sonication. A

custom-made stereotactic frame was designed to hold the transducer and provide fixed and 3-D translational/rotational positioning of the transducer. In this study, the image guidance procedure was replaced by self-designed stereotactic positioning combined with *a priori* knowledge of swine brain anatomy [26] to direct the ultrasound beam to its target position. Three different BBB-opening patterns were induced to investigate whether focal beam scanning could cover the volume of different target regions. In pattern 1, FUS was delivered to a single focal point driven at a single frequency of 400 kHz (pressures = 0.52/0.78 MPa; burst length = 10 ms, PRF = 1 Hz, total duration = 30 s) or 600 kHz (pressure = 0.52 MPa; burst length = 10 ms, PRF = 1 Hz, total duration = 30 s) [26]. In pattern 2, we delivered 3 × 3 sonication points via fast scanning with adjacent focal point spacing of 7 mm at frequency of 600 kHz (pressure = 0.52 MPa; burst length = 10 ms, PRF = 9 s, total duration = 30 s). Since the single 600-kHz 0.52-MPa exposure can induce a 6–8 mm BBB-opened dimension in cross section, it is expected that the mutual overlap produced with this spacing induced at least a $20 \times 20\,\text{mm}^2$ BBB-opened dimension in cross section, similar to the scheme used in recent large-animal studies [25], [26]. In pattern 3, FUS was steered to a single focal point, but with mixed frequencies of 400 and 600 kHz (pressure = 0.52 MPa; burst length = 10 ms, PRF = 1 s, total duration = 30 s; randomly-selected 128 elements were driven at 400 kHz, and the others were driven at 600 kHz; elements driven at 600 kHz were recalibrated to reach the overall 0.52-MPa exposure level).

G. Spectrophotometric Quantification of Evans Blue Dye and Histological Examination

The extent of FUS-BBB opening was assessed by measuring the penetration and deposition of Evans blue dye (EB; Molecular weight of 960 Da and becomes 60–70 kDa when bounds to serum albumin), which cannot normally penetrate the BBB. We previously demonstrated that spectrophotometry provides accurate quantitative information of EB penetration and correlates well with Gd-DTPA leakage as monitored by MRI [36]. After FUS exposure, EB (3% in saline) was intravenously injected (2 mg/kg) and the animals were sacrificed 4 h later by decapitation. For each FUS exposure pattern, the EB-stained brain tissues were collected and then homogenized, weighed, and placed in formamide (1 ml/100 mg) at 60 °C for 24 h. Extracted samples were centrifuged for 20 min at 14000 r/min. The concentration of dye extracted from each brain was determined spectrophotometrically at 620 nm by comparison with a standard graph created by recording optical densities from serial dilutions of EB in 0.9% sodium chloride solution. EB tissue content was quantified using a linear regression standard curve derived from seven concentrations of the dye. To histologically evaluate the applied FUS exposure among FUS exposure patterns, 5–20 frozen sections (10 μm thick) covering the exposure regions were stained with hematoxylin and eosin (HE). Under examination by light microscopy, the occurrence of erythrocyte extravasations (defined as the identification of grouped erythrocytes) was evaluated. Massive erythrocyte extravasation in brain parenchyma after FUS-BBB opening procedure was considered to be a hazardous complication [3], [4], [37].

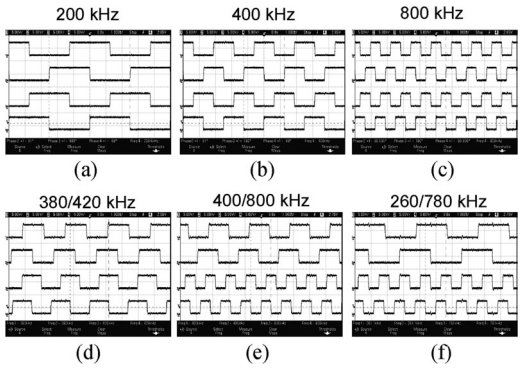

Fig. 4. TTL phasing signal samples generated from the control kernel. (a)–(c) Four phasing signals with adjacent phases designated to be 0°, 90°, 180°, and 270° at operating frequencies of (a) 200 kHz, (b) 400 kHz, and (c) 800 kHz. (d)–(f) TTL phasing signals when operating simultaneously at two different frequencies; (d) 400/800 kHz to demonstrate the simultaneous generation of baseband frequency along with its second harmonic; (e) 380/420 kHz to demonstrate beat frequency generation; (f) 260/780 kHz to demonstrate simultaneous generation of baseband frequency along with its third harmonic frequency.

III. Results

A. Control Kernel Testing

When operating at single-frequency output, the multiple channel system generated stable phasing TTL signals over a wide range of designated frequencies [200–800 kHz; Fig. 4(a)–(c)]. The measured frequency discrepancy of TTL signal was less than 0.08% (corresponding to phase error $< 0.18°$). We also investigated the capability of the system to generate dual-frequency simultaneous phasing TTL output signals [see Fig. 4(d)–(f)]. The system could generate a small beating frequency between the two designated frequencies, for example, a beat frequency of 40 kHz between 380 and 420 kHz [see Fig. 4(d)] [38], [39], and can be applied to both narrowband piezoelectric ceramics or wideband piezocomposite materials. We also demonstrated the simultaneous output of a center frequency and second harmonic frequency [400/800 kHz; Fig. 4(e)]. To support this type of ultrasound energy exposure, two piezoelectric ceramics with different center frequencies should be selected to match the designated output frequencies, or a large bandwidth transducer can be used to cover the frequency range. This type of excitation could potentially be used for cavitation-enhanced therapy [30], [34]. Moreover, a typical transducer features base mode (i.e., baseband frequency) and third mode (i.e., third harmonic frequency) excitation [34], [40]. Fig. 4(h) shows that the simultaneous center frequency/third harmonic frequency output can be applied to excite the same ceramic transducer in its baseband mode or third harmonic mode. The measured frequency discrepancy was higher in the dual than in the single-frequency generation mode, but still within the acceptable range (a maximum of 1.67 ± 1.06 kHz), with measured output frequency discrepancy $< 0.5\%$ (corresponding to a phase error of 1.5°).

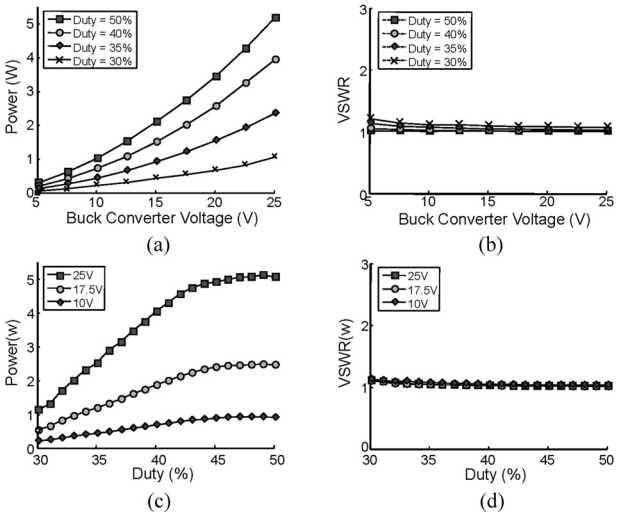

Fig. 5. (a, b) Measured forward/reflected electrical power and the corresponding VSWR when the power was controlled by the MCU-controlled dc-to-dc buck converter output voltage (with the TTL signal duty cycle varying from 30% to 50%); (c, d) Measured forward/reflected electrical power and the corresponding VSWR when the power was controlled by the TTL signal duty cycle output voltage (with the buck converter output voltage varying from 10 to 25 V). Maximal electrical power transfer to the transducer (efficiency = 100%) corresponds to an ideal VSWR of 1. All measured VSWR values were < 1.22, which was equivalent to an electrical power transfer efficiency $> 99\%$.

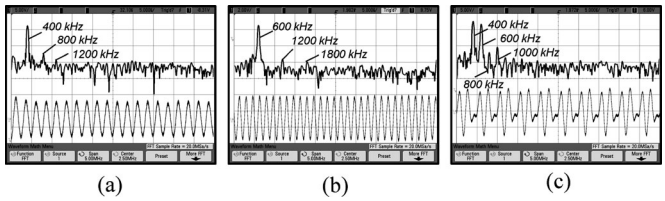

Fig. 6. Measured signals and corresponding spectrums at geometrical center when operating the driving system at (a) 400 kHz alone, (b) 600 kHz alone, or (c) concurrently at 400/600 kHz. Time-domain scale: 5 μs/Div in horizontal axis and 5 V/Div in vertical axis; spectral scale: 500 kHz/Div in horizontal axis and 20 dB/Div in vertical axis.

B. RF Driving Module Testing

The electrical output can be regulated either by the MCU-controlled buck converter voltage level [see Fig. 5(a) and (b)] or by the duty cycle of the TTL phasing signal from the FPGA output end [see Fig. 5(c) and (d)]. A wide range of power (0–5 W per channel with 8-bit resolution) could be produced by either power control route. The electrical power transmission efficiency was maintained at higher than 99.5%. The power could also be regulated to allow dynamic generation of burst-tone mode high-voltage output and frequencies which varied over time in each sonication. The measured maximum rise time of power regulation was 146 μs/V for an RF output with peak-to-peak voltage of 150 V, which was sufficient for stabilizing the output power of ms-level burst mode RF signal excitation.

C. Ultrasound Pressure Distribution Measurement

Fig. 6 shows PVDF-hydrophone received signals and the corresponding spectrums at single-frequency excitations (either at 400 and 600 kHz) as well as 400/600-kHz dual-frequency excitations when focused at geometrical center. With 400-kHz or 600-kHz excitation, a single-frequency sinusoidal signal was observed on the oscilloscope. Only 400 kHz (or 600 kHz) and its corresponding harmonic components were observed in the frequency domain spectrum [see Fig. 6(a) and (b)]. When 400/600-kHz excitation was used, cross-modulated time-domain signals were observed, and frequency components of $400 \times m \pm 600 \times n$ kHz could be observed where m and n were integers [see Fig. 6(c)].

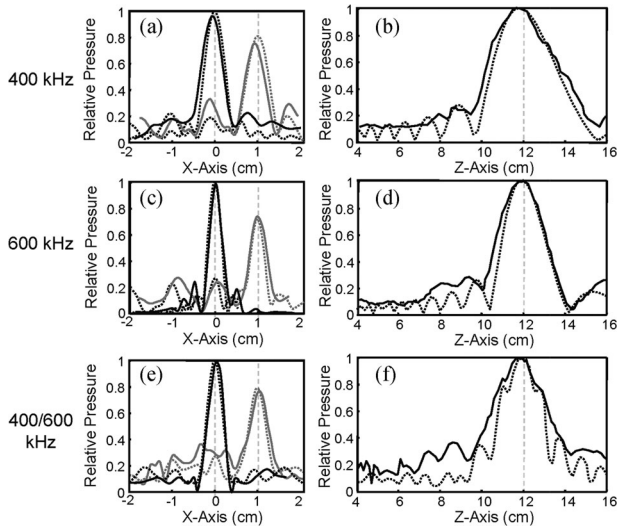

Fig. 7. Theoretically predicted and measured pressure distributions along the axial direction (with radial steering at center and 10-mm off center; left) and radial direction (with axial focusing at 120 mm; right) when operating the driving system at (a, b) 400 kHz alone, (c, d) 600 kHz alone, or in (e, f) 400/600 kHz dual-frequency mode. Theoretical values were plotted with dot lines and measured values were plotted with solid lines.

Fig. 7 shows the measured 2-D pressure distributions at 400-kHz or 600-kHz single-frequency excitation as well as 400/600-kHz dual-frequency excitation when focused at geometrical center (without giving relative phases among elements), steered along one direction off-center (10 mm), or with 2-D steering off-center (10 mm along both directions). It was observed that 600-kHz and 400/600-kHz excitation provided a sharper distribution in the –3 dB dimension than in the 400-kHz one (3.1 and 2.9 mm at 600-kHz and 400/600-kHz excitation, respectively, compared to 3.5 mm at 400-kHz excitation).

Fig. 8 shows the comparison of the simulated and measured pressure profiles, either along the radial direction [see Fig. 8(a), (c), and (e)] or radial-axial direction [Fig. 8(b), (d), and (f)] with the frequency set to 400, 600, or dual 400/600 kHz. Simulated predictions of the distributions and magnitudes of the pressure correlated well with the actual pressure measurements. Along the radial-direction steering shift, the measured pressure decayed 22.4%, 23.2%, and 23.4% when steering 10-mm off-center at 400, 600, and dual 400/600-kHz excitations, respectively. In the focal plane, the side lobe magnitudes were all -6 dB (i.e., 50%) less than the focal point for all frequency excitations. Thus, the phased array provided well-concentrated ultrasonic energy when steering 10-mm off the geometrical center in the radial direction.

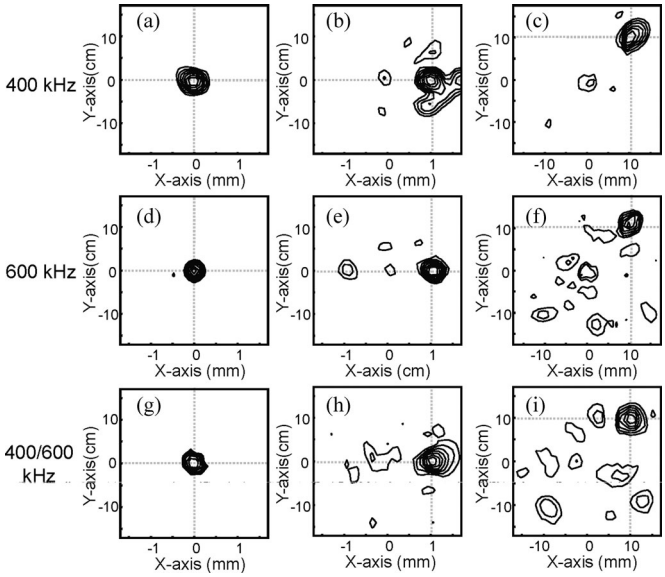

Fig. 8. Measured 2-D pressure distribution at 400 kHz alone, 600 kHz alone, or 400/600 kHz dual-frequency operation when steering at geometrical center (left), 10-mm off center (along x direction; middle), and 10-mm off center (2-D steering; right). Contours represent 10% increments of pressure level, from 30% to 90% on a linear scale.

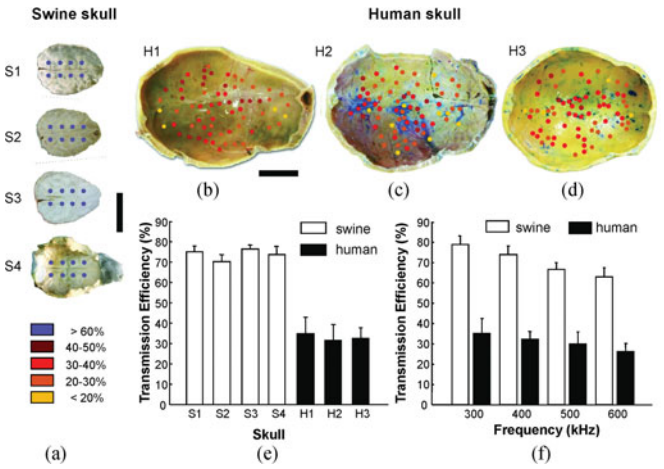

Fig. 9. (a) Distributions of measured acoustic transmission locations on four swine skulls (bar = 5 cm); (b)–(d) distributions of measured acoustic transmission locations on three human cadaver skulls (bar = 5 cm); (e) normalized pressure transmission efficiency when measured in the skull cavity of four swine and three human cadaver skulls (measured at 400 kHz); (f) normalized pressure transmission efficiency when measured in swine skull S4 and human cadaver skull H3 with a driving frequency of 300–600 kHz.

Next, we measured the transmission efficiency when FUS energy was transmitted through swine and human skulls. For four swine skulls (see Fig. 9(a), S1–S4), the pressure transmission efficiency (compared to free-field measurement) was estimated to be 75.1 $\pm$ 2.9% (S1), 70.4 $\pm$ 3.3% (S2), 76.5 $\pm$ 2.1% (S3), and 73.7 $\pm$ 4.0% (S4) at 400 kHz [see Fig. 9(e)]. In addition, the pressure transmission efficiency measured from three human skulls (see Fig. 9(b)–(d), H1–H3) was 34.7 $\pm$ 8.3% (H1), 31.5 $\pm$ 7.9% (H2), and 32.4 $\pm$ 5.3% (H3) at 400 kHz [see Fig. 9(e)]. The pressure transmission efficiency was also found to be dependent on operating frequency, and decreased from 79 $\pm$ 10% at 300 kHz to 63 $\pm$ 10.2% at 600 kHz in swine skull (S4), and from 35.2 $\pm$ 7.4% at 300 kHz to 24.8 $\pm$ 4.2% at 600 kHz in human skull [H3; Fig. 9(f)].

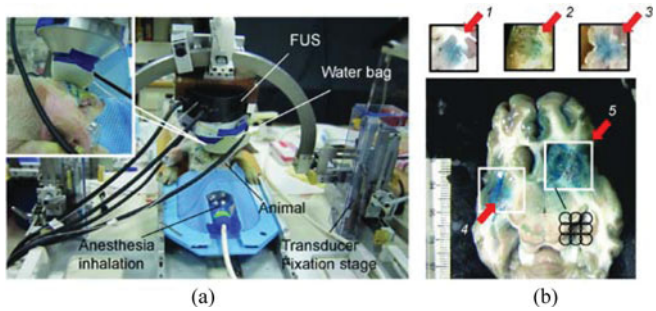

Fig. 10. (a) Setup of the large-animal experiment. (b) Swine brain sections and EB-stained tissue samples after receiving FUS exposure. (1) 400 kHz, single, 0.52 MPa; (2) 600 kHz, single, 0.52 MPa; (3) 400/600 kHz, single, 0.52 MPa; (4) 400 kHz, single, 0.78 MPa; (5) 400 kHz, 3 $\times$ 3 multiple exposure, 0.52 MPa.

D. In Vivo Experiments

The setup of the large-animal experiments is shown in Fig. 10(a). The animal was placed in a prone position beneath the transducer. The transducer was covered by a polyethylene bag filled with degassed water to serve as an acoustic coupling, and was tightly attached to the shaved animal scalp. The transducer was fixed on the custom-made stereotactic frame so that FUS energy could be steered to the designated target position. FUS exposure was delivered in different patterns to induce different scales of BBB opening. Typical BBB-opened and EB-stained tissue sections induced by different exposure patterns are shown in Fig. 10(b). The 400-kHz, 0.52-MPa exposure induced a 8-mm-wide BBB-opened and EB-stained tissue region [see Fig. 10(b), tissue sample 1] and the 600-kHz 0.52-MPa exposure induced a 6-mm one (tissue sample 2). The 400/600-kHz exposure seemed to create a deeper-stained pattern in color than either 400 or 600 kHz exposures (see Fig. 10(b), tissue sample 3).

BBB opening with an exposure at increased pressure was also demonstrated. Single point 0.78-MPa, 400-kHz exposure [see Fig. 10(b), tissue sample 4] resulted in a wider (and more deeply stained) BBB-opened region which appeared more irregular in shape (7 mm wide and 15 mm long in this example). Conversely, to test the capability of creating a square-shaped 20 $\times$ 20 mm^2 BBB-opened region, a 0.52-MPa, 400-kHz multiple-point exposure was performed as an example [see Fig. 10(b), tissue sample 5]. In addition to the gross observation of EB-stained brain sections, we spectrophotometrically quantified the concentrations of deposited EB dye in the BBB-opened animal brain (see Fig. 11 and Table I). A control brain was used as a reference for the lowest EB concentration (0.37 $\pm$ 0.13 μM). EB concentration showed a twofold increase (0.7 $\pm$ 0.13 μM) for a 0.52-MPa 400-kHz single-point exposure, and a smaller increase (0.66 $\pm$ 0.36 μM) for a 0.52-MPa 600-kHz single-point exposure. The EB concentration was significantly increased when the pressure was increased to 0.78 MPa (1.7 $\pm$ 0.5 μM; 400-kHz single-point exposure). Interestingly, we observed that a wider BBB-opened region was created by a 0.52-MPa 400-kHz multiple-point

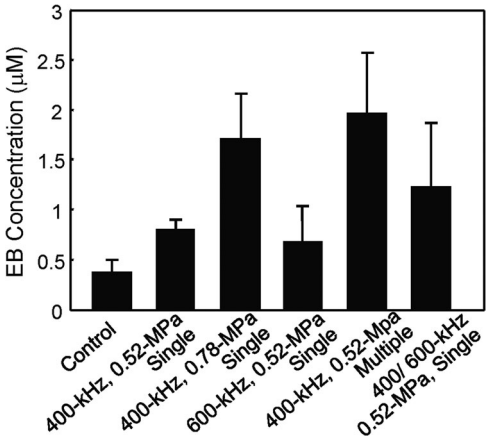

Fig. 11. Comparison of the measured Evans blue dye concentrations for different FUS exposure conditions. EB = Evans blue.

TABLE I
SUMMARY OF THE MEASURED EVANS BLUE DYE CONCENTRATIONS AT FUS-EXPOSED TISSUES FOR DIFFERENT SONICATION CONDITIONS

Experimental group (Animal No.)	EB concentration (individual; μM)	EB concentration (Mean ± S.D.; μM)
Control (n = 5)	0.44/ 0.30/ 0.22/ 0.33/ 0.55	0.37 ± 0.13
400 kHz, single, 0.52 MPa (n = 8)	0.62/ 0.50/ 0.83/ 0.71/ 0.72/ 0.83/ 0.72/ 0.88	0.73 ± 0.12
400 kHz, single, 0.78 MPa (n = 5)	1.70/ 2.60/ 1.05/ 2.30/ 2.10	1.95 ± 0.60
600 kHz, single, 0.52 MPa (n = 5)	0.50/ 0.56/ 0.58/ 0.70/ 0.39/0.70	0.67 ± 0.36
400 kHz, multiple, 0.52 MPa (n = 5)	1.50/ 1.10/ 1.46/ 2.30/ 2.14	1.70 ± 0.46
400/ 600 kHz, single, 0.52 MPa (n = 6)	0.63/ 1.01/ 0.74/ 2.10/ 1.25/ 1.60	1.22 ± 0.64

EB = Evans blue; SF = single frequency; DF = dual frequency; single = single point exposure; multiple = 3×3 matrix exposure.

exposure (3 × 3 points). The EB concentration was also significantly increased to a fivefold higher level than control (1.95 ± 0.61 μM), suggesting that focal point overlapping provided further improvement of EB penetration. On the other hand, 0.52-MPa 400/600-kHz single-point exposure resulted in higher EB penetration (1.22 ± 0.64 μM) than any single-frequency exposure at the same pressure level. This suggested that dual-frequency FUS-BBB opening provides an alternative to locally increase drug penetration in addition to existing strategies of either increasing acoustic pressure or performing multiple overlapping exposures.

Typical HE-stained brain sections are shown in Fig. 12, and the occurrence of erythrocyte extravasations among FUS exposure patterns is summarized in Table II. Among all HE slides of 0.52-MPa single-frequency single-point exposures, a minority of the brain sections (15.3% at 400 kHz and 10.0% at 600 kHz) showed grouped extravasated erythrocytes. At increasing pressure (0.78 MPa), the occurrence of extravasations was significantly increased (66.7%). Applying 3 × 3 multiple exposures also induced a high occurrence of extravasations (76.7%), implying that the pressure level in multiple exposures should be

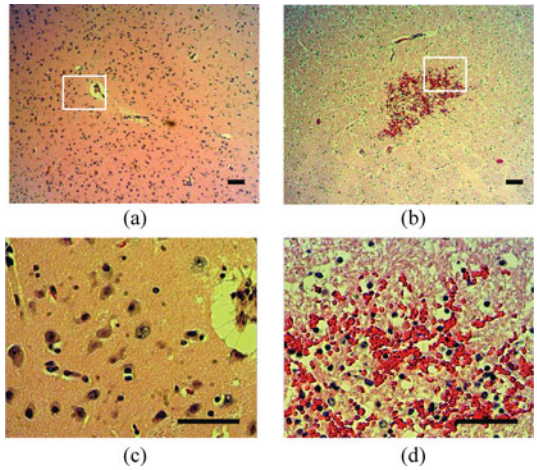

Fig. 12. HE stained brain sections. (a, c) Intact brain tissues after FUS exposure, 40× and 200× (400/600 kHz, single, 0.52 MPa; subcortical region). (b, d) Identified grouped erythrocyte extravasations after FUS exposure, 40× and 200× (400 kHz, single, 0.78 MPa; subcortical region). Bar = 100 μm.

TABLE II
SUMMARY OF HISTOLOGICAL EXAMINATION

Exposure	W/O erythrocyte Extravasations	Grouped erythrocyte Extravasations	Sample No. (Animal No.)
400 kHz, single, 0.52 MPa	70 (84.7%)	15 (15.3%)	85 (5)
400 kHz, single, 0.78 MPa	15 (33.3%)	30 (66.7%)	45 (6)
600 kHz, single, 0.52 MPa	54 (90.0%)	6 (10%)	60 (2)
400 kHz, multiple, 0.52 MPa	35 (23.3%)	115 (76.7%)	150 (5)
400/ 600 kHz, single, 0.52 MPa	70 (87.5%)	10 (12.5%)	80 (6)
		Total	420 (24)

SF = single frequency; DF = dual frequency; single = single point exposure; multiple = 3×3 matrix exposure.

reoptimized when intending to induce a large BBB-opened region. Of note, dual-frequency FUS exposure showed a similar level of extravasations (12.5%), implying that it did not further increase erythrocyte extravasation above the level obtained with traditional single-frequency exposures.

IV. DISCUSSION

Our preliminary animal experiments demonstrated the feasibility of disrupting the BBB through an intact animal skull, either in single or scanned target regions. Based on our transskull pressure measurement, *in vivo* animal experiments, as well as previous studies of the efficiency of low-frequency ultrasound to penetrate the skull [27], we assume that FUS produced by our system will penetrate through the human skull. We successfully demonstrated that dual-frequency excitation could be steered spatially, and could also induce efficient targeting of BBB opening with improved EB penetration compared to single-frequency

exposure. Unlike enhanced delivery obtained through increasing the pressure or performing repetitive/overlapped exposures, dual-frequency exposure appears to increase BBB permeability without worsening erythrocyte extravasation, therefore providing a new direction toward optimizing FUS-based brain drug delivery. This study therefore provides useful design experience of a multifrequency ultrasound phased array driving system, and may also contribute toward the future design of arrays using various combinations of frequencies to improve transcranial FUS brain-drug delivery efficiency.

Our novel FUS phased-array driving system was capable of simultaneously exciting dual frequency output, thus demonstrating the feasibility of multiple frequency FUS exposure. Two distinct frequencies, both within the transducer bandwidth, could be simultaneously driven. In addition, beat-frequency generation was feasible ($\pm$20 kHz off the center frequency). Beat frequency generation was previously reported to be useful for characterizing tissue properties or providing bubble/cavitation feedback [41], [42], and could therefore be further explored as an ultrasound-stimulated acoustic emission technique capable of monitoring BBB opening and drug delivery. Subharmonic, harmonic, or superharmonic frequency components were recently shown to accompany the BBB-opening process, and are likely to correlate with inertial or stable bubble cavitation. Since microbubble cavitation is the major mechanism for the induction of BBB opening, it could be used for direct monitoring of BBB-opening during FUS exposure, and possibly also to control the BBB-opening process [43]–[45]. In addition, the frequency component could perhaps be manipulated to induce, enhance, or manipulate FUS BBB opening. We demonstrated that, within the transducer bandwidth (400–800 kHz), it is also possible to provide main/subharmonic, main/superharmonic, or main/harmonic dual frequency excitation. These different kinds of dual frequency excitations could also serve as a useful platform to further investigate the benefits of dual-frequency exposure on brain drug delivery. In addition, the dual- or multiple-frequency excitation in this application may also have the potential to reduce the standing wave problem [46], that could possibly induce unwanted off-target brain lesions [24], [47]. Our preliminary experiments demonstrated that at identical pressure levels, EB penetration appeared to be superior after dual-frequency FUS-BBB opening compared to single-frequency treatment. Dual-frequency FUS-BBB opening may thus involve enhanced cavitation, especially stable cavitation, since 600 kHz is the ultraharmonic component of 400 kHz and is characteristic of stable cavitation. The exact mechanism of dual-frequency FUS-enhanced BBB opening needs to be further investigated.

Depending on the type of medical device and desired market, regulatory agencies enforce EMC standards that greatly impact the design and marketability of electromedical devices. EMC testing, which is required in most markets, helps to demonstrate that the product's emission quality does not affect the normal operation of other medical devices in the same environment. EM immunity tests also help to justify that EM emissions from devices do not affect the normal operation of the designed system. For medical devices, EMC testing is primarily considered a safety issue. High risk electrical and electronic medical devices can be affected by EMI which can lead to potential malfunctioning causing inconvenient or even life threatening situations. IEC 60601-1-2 is a "pointer" standard that provides comprehensive test levels and defines the pass/fail criteria that covers CISPR 11 for emissions and various IEC 61000 standards for immunity.

The emphasis of our study was on the design of an ultrasound phased-array driving system; however, development of an image-guided procedure (such as MRI guidance [4]) is also essential so that FUS energy can be correctly delivered to the target position. Currently, the designed system does not provide MR compatibility because: 1) the current coaxial cable length is limited (3 m/channel); and 2) the coaxial cable does not provide sufficient EM shielding and causes sustainable EM interference to MRI. However, we demonstrated that EM conduction interference can be substantially suppressed with the added EMC design, thus providing the opportunity to further improve MR compatibility, which will be investigated in our future work. An alternative image guidance system without requiring MR compatibility is to use our previously proposed scheme which incorporates a neuronavigation system to perform FUS exposure guidance [26].

V. Conclusion

In this study, we presented a prototype design of a 256-channel ultrasound phased-array system to perform localized BBB disruption. To our knowledge, it is the first prototype of a phased array that demonstrates the feasibility of simultaneous, dual-frequency exposure from an ultrasound array. The large animal experiments confirmed the feasibility of inducing a large BBB-opened region by electronic scanning via phase switching control, and also demonstrated the potential to enhance the BBB-opening effect through dual-frequency FUS exposure. This study is expected to contribute to the design of an advanced ultrasound phased-array system for future clinical applications of FUS-induced brain drug delivery.

References

[1] K. Hynynen, N. McDannold, N. A. Sheikov, F. A. Jolesz, and N. Vykhodtseva, "Local and reversible blood-brain barrier disruption by noninvasive focused ultrasound at frequencies suitable for trans-skull sonications," *Neuroimage*, vol. 24, pp. 12–20, Jan. 1, 2005.

[2] N. McDannold, N. Vykhodtseva, S. Raymond, F. A. Jolesz, and K. Hynynen, "MRI-guided targeted blood-brain barrier disruption with focused ultrasound: Histological findings in rabbits," *Ultrasound Med. Biol.*, vol. 31, pp. 1527–1537, Nov. 2005.

[3] K. Hynynen, N. McDannold, N. Vykhodtseva, and F. A. Jolesz, "Noninvasive opening of BBB by focused ultrasound," *Acta Neurochirurgica Suppl.*, vol. 86, pp. 555–558, 2003.

[4] K. Hynynen, N. McDannold, N. Vykhodtseva, and F. A. Jolesz, "Noninvasive MR imaging-guided focal opening of the blood-brain barrier in rabbits," *Radiology*, vol. 220, pp. 640–646, Sep. 2001.

[5] L. H. Treat, N. McDannold, Y. Zhang, N. Vykhodtseva, and K. Hynynen, "Improved anti-tumor effect of liposomal doxorubicin after targeted blood-brain barrier disruption by MRI-guided focused ultrasound in rat glioma," *Ultrasound Med. Biol.*, vol. 38, pp. 1716–1725, Oct. 2012.

[6] H. L. Liu, H. W. Yang, M. Y. Hua, and K. C. Wei, "Enhanced therapeutic agent delivery through magnetic resonance imaging-monitored focused ultrasound blood-brain barrier disruption for brain tumor treatment: An overview of the current preclinical status," *Neurosurg. Focus*, vol. 32, p. E4, Jan. 2012.

[7] H. L. Liu, M. Y. Hua, P. Y. Chen, P. C. Chu, C. H. Pan, H. W. Yang, C. Y. Huang, J. J. Wang, T. C. Yen, and K. C. Wei, "Blood-brain barrier

disruption with focused ultrasound enhances delivery of chemotherapeutic drugs for glioblastoma treatment," *Radiology*, vol. 255, pp. 415–425, May 2010.

[8] P. H. Hsu, K. C. Wei, C. Y. Huang, C. J. Wen, T. C. Yen, C. L. Liu, Y. T. Lin, J. C. Chen, C. R. Shen, and H. L. Liu, "Noninvasive and targeted gene delivery into the brain using microbubble-facilitated focused ultrasound," *PLoS One*, vol. 8, p. e57682, 2013.

[9] E. Thevenot, J. F. Jordao, M. A. O'Reilly, K. Markham, Y. Q. Weng, K. D. Foust, B. K. Kaspar, K. Hynynen, and I. Aubert, "Targeted delivery of self-complementary adeno-associated virus serotype 9 to the brain, using magnetic resonance imaging-guided focused ultrasound," *Hum. Gene Therapy*, vol. 23, pp. 1144–1155, Nov. 2012.

[10] M. Kinoshita, N. McDannold, F. A. Jolesz, and K. Hynynen, "Noninvasive localized delivery of herceptin to the mouse brain by MRI-guided focused ultrasound-induced blood-brain barrier disruption," *Proc. Natl. Acad. Sci. USA*, vol. 103, pp. 11719–11723, Aug. 1, 2006.

[11] A. Burgess, C. A. Ayala-Grosso, M. Ganguly, J. F. Jordao, I. Aubert, and K. Hynynen, "Targeted delivery of neural stem cells to the brain using MRI-guided focused ultrasound to disrupt the blood-brain barrier," *PLoS One*, vol. 6, p. e27877, 2011.

[12] M. T. Buchanan and K. Hynynen, "Design and experimental evaluation of an intracavitary ultrasound phased array system for hyperthermia," *IEEE Trans. Biomed. Eng.*, vol. 41, no. 12, pp. 1178–1187, Dec. 1994.

[13] D. R. Daum and K. Hynynen, "A 256-element ultrasonic phased array system for the treatment of large volumes of deep seated tissue," *IEEE Trans. Ultrason., Ferroelectr., Freq. Control*, vol. 46, no. 5, pp. 1254–1268, Sep. 1999.

[14] G. T. Clement, J. Sun, T. Giesecke, and K. Hynynen, "A hemisphere array for non-invasive ultrasound brain therapy and surgery," *Phys. Med. Biol.*, vol. 45, pp. 3707–3719, Dec. 2000.

[15] M. Pernot, J. F. Aubry, M. Tanter, A. L. Boch, F. Marquet, M. Kujas, D. Seilhean, and M. Fink, "In vivo transcranial brain surgery with an ultrasonic time reversal mirror," *J. Neurosurg.*, vol. 106, pp. 1061–1066, Jun. 2007.

[16] G. T. Clement, P. J. White, R. L. King, N. McDannold, and K. Hynynen, "A magnetic resonance imaging-compatible, large-scale array for transskull ultrasound surgery and therapy," *J. Ultrasound Med.*, vol. 24, pp. 1117–1125, Aug. 2005.

[17] K. Hynynen, G. T. Clement, N. McDannold, N. Vykhodtseva, R. King, P. J. White, S. Vitek, and F. A. Jolesz, "500-element ultrasound phased array system for noninvasive focal surgery of the brain: A preliminary rabbit study with ex vivo human skulls," *Magn. Reson. Med.*, vol. 52, pp. 100–107, Jul. 2004.

[18] K. Hynynen, A. Darkazanli, E. Unger, and J. F. Schenck, "MRI-guided noninvasive ultrasound surgery," *Med. Phys.*, vol. 20, pp. 107–115, Jan./Feb. 1993.

[19] N. T. Sanghvi and R. H. Hawes, "High-intensity focused ultrasound," *Gastrointestinal Endoscopy Clin. North Am.*, vol. 4, pp. 383–395, Apr. 1994.

[20] G. ter Haar, "Ultrasound focal beam surgery," *Ultrasound Med. Biol.*, vol. 21, pp. 1089–1100, 1995.

[21] N. McDannold, N. Vykhodtseva, F. A. Jolesz, and K. Hynynen, "MRI investigation of the threshold for thermally induced blood-brain barrier disruption and brain tissue damage in the rabbit brain," *Magn. Reson. Med.*, vol. 51, pp. 913–923, May 2004.

[22] H. L. Liu, N. McDannold, and K. Hynynen, "Focal beam distortion and treatment planning in abdominal focused ultrasound surgery," *Med. Phys.*, vol. 32, pp. 1270–1280, May 2005.

[23] H. L. Liu, H. W. Chen, Z. H. Kuo, and W. C. Huang, "Design and experimental evaluations of a low-frequency hemispherical ultrasound phased-array system for transcranial blood-brain barrier disruption," *IEEE Trans. Biomed. Eng.*, vol. 55, no. 10, pp. 2407–2416, Oct. 2008.

[24] J. Song, A. Pulkkinen, Y. Huang, and K. Hynynen, "Investigation of standing-wave formation in a human skull for a clinical prototype of a large-aperture, transcranial MR-guided focused ultrasound (MRgFUS) phased array: An experimental and simulation study," *IEEE Trans. Biomed. Eng.*, vol. 59, no. 2, pp. 435–444, Feb. 2012.

[25] N. McDannold, C. D. Arvanitis, N. Vykhodtseva, and M. S. Livingstone, "Temporary disruption of the blood-brain barrier by use of ultrasound and microbubbles: Safety and efficacy evaluation in rhesus macaques," *Cancer Res.*, vol. 72, pp. 3652–3653, 2012.

[26] K. C. Wei, H. C. Tsai, Y. J. Lu, H. W. Yang, M. Y. Hua, M. F. Wu, P. Y. Chen, C. Y. Huang, T. C. Yen, and H. L. Liu, "Neuronavigation-guided focused ultrasound-induced blood-brain barrier opening: A preliminary study in swine," *AJNR Am. J. Neuroradiol.*, vol. 34, pp. 115–120, Jan. 2013.

[27] S. Wang, B. Huang, Y. Wang, and L. Liao, "Comparison of enhancement of pentachlorophenol sonolysis at 20 kHz by dual-frequency sonication," *Ultrason. Sonochem.*, vol. 13, pp. 506–510, Sep. 2006.

[28] H. L. Liu and C. M. Hsieh, "Single-transducer dual-frequency ultrasound generation to enhance acoustic cavitation," *Ultrason. Sonochem.*, vol. 16, pp. 431–438, Mar. 2009.

[29] D. Zhang, X. Xi, Z. Zhang, X. Gong, G. Chen, and J. Wu, "A dual-frequency excitation technique for enhancing the sub-harmonic emission from encapsulated microbubbles," *Phys. Med. Biol.*, vol. 54, pp. 4257–4272, Jul. 7, 2009.

[30] H. Hasanzadeh, M. Mokhtari-Dizaji, S. Z. Bathaie, Z. M. Hassan, V. Nilchiani, and H. Goudarzi, "Enhancement and control of acoustic cavitation yield by low-level dual frequency sonication: A subharmonic analysis," *Ultrason. Sonochem.*, vol. 18, pp. 394–400, Jan. 2011.

[31] A. Brotchie, R. Mettin, F. Grieser, and M. Ashokkumar, "Cavitation activation by dual-frequency ultrasound and shock waves," *Phys. Chem. Chem. Phys.*, vol. 11, pp. 10029–10034, Nov. 21, 2009.

[32] C. M. Schoellhammer, B. E. Polat, J. Mendenhall, R. Maa, B. Jones, D. P. Hart, R. Langer, and D. Blankschtein, "Rapid skin permeabilization by the simultaneous application of dual-frequency, high-intensity ultrasound," *J. Control Release*, vol. 163, pp. 154–160, Oct. 28, 2012.

[33] M. A. Diaz de la Rosa, G. A. Husseini, and W. G. Pitt, "Comparing microbubble cavitation at 500 kHz and 70 kHz related to micellar drug delivery using ultrasound," *Ultrasonics*, vol. 53, pp. 377–386, Feb. 2013.

[34] N. McDannold, N. Vykhodtseva, and K. Hynynen, "Targeted disruption of the blood-brain barrier with focused ultrasound: Association with cavitation activity," *Phys. Med. Biol.*, vol. 51, pp. 793–807, Feb. 21, 2006.

[35] H. L. Liu, C. L. Hsu, S. M. Huang, and Y. W. Hsi, "Focal beam distortion and treatment planning for transrib focused ultrasound thermal therapy: A feasibility study using a two-dimensional ultrasound phased array," *Med. Phys.*, vol. 37, pp. 848–860, Feb. 2010.

[36] P. C. Chu, W. Y. Chai, H. Y. Hsieh, J. J. Wang, S. P. Wey, C. Y. Huang, K. C. Wei, and H. L. Liu, "Pharmacodynamic analysis of magnetic resonance imaging-monitored focused ultrasound-induced blood-brain barrier opening for drug delivery to brain tumors," *Biomed. Res. Int.*, vol. 2013, p. 627496, 2013.

[37] H. L. Liu, Y. Y. Wai, W. S. Chen, J. C. Chen, P. H. Hsu, X. Y. Wu, W. C. Huang, T. C. Yen, and J. J. Wang, "Hemorrhage detection during focused-ultrasound induced blood-brain-barrier opening by using susceptibility-weighted magnetic resonance imaging," *Ultrasound Med. Biol.*, vol. 34, pp. 598–606, Apr. 2008.

[38] M. Fatemi and J. F. Greenleaf, "Ultrasound-stimulated vibro-acoustic spectrography," *Science*, vol. 280, pp. 82–85, Apr. 3, 1998.

[39] J. S. Thierman and K. Hynynen, "Ultrasound acoustic stimulated emission for controlling thermal surgery," in *Proc. IEEE Int. Ultrason. Symp.*, 1999, pp. 1397–1400.

[40] G. ter Haar, D. Sinnett, and I. Rivens, "High intensity focused ultrasound—A surgical technique for the treatment of discrete liver tumours," *Phys. Med. Biol.*, vol. 34, pp. 1743–1750, Nov. 1989.

[41] S. Chen, R. Kinnick, J. F. Greenleaf, and M. Fatemi, "Difference frequency and its harmonic emitted by microbubbles under dual frequency excitation," *Ultrasonics*, vol. 44, no. Suppl 1, pp. e123–e126, Dec. 22, 2006.

[42] M. Fatemi and J. F. Greenleaf, "Vibro-acoustography: An imaging modality based on ultrasound-stimulated acoustic emission," *Proc. Natl. Acad. Sci. USA*, vol. 96, pp. 6603–6608, Jun. 8, 1999.

[43] M. A. O'Reilly and K. Hynynen, "A PVDF receiver for ultrasound monitoring of transcranial focused ultrasound therapy," *IEEE Trans. Biomed. Eng.*, vol. 57, no. 9, pp. 2286–2294, Sep. 2010.

[44] C. D. Arvanitis, M. S. Livingstone, N. Vykhodtseva, and N. McDannold, "Controlled ultrasound-induced blood-brain barrier disruption using passive acoustic emissions monitoring," *PLoS One*, vol. 7, p. e45783, 2012.

[45] M. A. O'Reilly and K. Hynynen, "Blood-brain barrier: Real-time feedback-controlled focused ultrasound disruption by using an acoustic emissions-based controller," *Radiology*, vol. 263, pp. 96–106, Apr. 2012.

[46] T. M. Huber, N. M. Beaver, and J. R. Helps, "Elimination of standing wave effects in ultrasound radiation force excitation in air using random

carrier frequency packets," *J. Acoust. Soc. Am.*, vol. 130, pp. 1838–1843, Oct. 2011.

[47] M. A. O'Reilly, Y. Huang, and K. Hynynen, "The impact of standing wave effects on transcranial focused ultrasound disruption of the blood-brain barrier in a rat model," *Phys. Med. Biol.*, vol. 55, pp. 5251–5267, Sep. 21, 2010.

Hao-Li Liu (M'07) received the Ph.D. degrees in electrical engineering from the National Taiwan University, Taipei, Taiwan, in 2003.

In 2004–2005, he was the Research Fellow in the Department of Radiology, Brigham and Women's Hospital, Harvard Medical School, Boston, MA, USA. He is currently a Professor and the Director in the Department of Electrical Engineering, Chang-Gung University, Taoyuan, Taiwan, and also the Adjunct Researcher of the Division of Medical Engineering Research, National Health Research Institutes, Miaoli, Taiwan. He is currently continuing research in ultrasound thermal therapy and its treatment planning/simulation, ultrasound-induced blood–brain barrier disruption for brain drug delivery, ultrasound phased-array design.

Dr. Liu is a member of the International Society of Therapeutic Ultrasound (ISTU). In 2010 and 2011, he received the Distinguished Tech-Coop Award and the Distinguished Research Award from Chang-Gung University, respectively. Also, in 2011, he received the Wu Ta-You Memorial Award from the National Science Council in Taiwan. In 2013, he received the Frederic Lizzi Award from the ISTU to acknowledge his significant research contributions to therapeutic ultrasound.

Chen-Kai Jan, photograph and biography not available at the time of publication.

Po-Chun Chu, photograph and biography not available at the time of publication.

Jhong-Cing Hong, photograph and biography not available at the time of publication.

Pei-Yun Lee, photograph and biography not available at the time of publication.

Jyh-Duen Hsu, photograph and biography not available at the time of publication.

Chung-Chih Lin, photograph and biography not available at the time of publication.

Chiung-Ying Huang, photograph and biography not available at the time of publication.

Pin-Yuan Chen, photograph and biography not available at the time of publication.

Kuo-Chen Wei, photograph and biography not available at the time of publication.